Digest Journal of Nanomaterials and Biostructures Vol. 16, No. 1, January - March 2021, p. 317 - 329

CLUSTERED ZnO NANOPARTICLES SYNTHESIZED VIA PRECIPITATION FOR PHOTOCATALYTIC DEGRADATION OF METHYL ORANGE AND GLYPHOSATE

S. SUJINNAPRAM[a], S. NILPHAI[b], S. MOUNGSRIJUN[a], S. KROBTHONG[a], S. WONGRERKDEE[a,*]
[a]*Department of Physics, Faculty of Liberal Arts and Science, Kasetsart University Kamphaeng Saen Campus, Nakhon Pathom 73140, Thailand*
[b]*Physics Program, Department of Science and Technology, Faculty of Liberal Arts and Science, Roi Et Rajabhat University, Roi Et 45120, Thailand*

Precipitation of clustered ZnO nanoparticles was performed from low-cost starting materials. Morphological and particle size analyses show the cluster formation accumulating with nanoparticles. Chemical composition detection refers the ZnO formation. Hexagonal wurtzite structures are confirmed with low crystal size, high dislocation density, and spherical growth. Optical band gap shows red shift affecting to low required activating energy for photocatalytic activity. Photocatalytic degradation of methyl orange and glyphosate presents degradation rate constants of 3.28×10^{-3} min^{-1} and 2.45×10^{-3} min^{-1}, respectively, which is caused by the synergy of small particle size, small crystal size, high dislocation density, and low optical band gap. Therefore, clustered ZnO nanoparticles were demonstrated as a potential photocatalytic material for the decomposition of methyl orange and glyphosate.

(Received October 26, 2020; Accepted March 17, 2021)

Keywords: ZnO, Nanoparticles, Photocatalytic degradation, Methyl orange, Glyphosate

1. Introduction

Wastewater is a serious problem that needs to be resolved to ensure good aquatic ecosystems [1] and a sustainable environment [2]. Most contaminants in wastewater are organic or inorganic materials such as metals [3], polymers, residues from chemical fertilizers [1], pharmaceuticals [4,5], textiles, pigments, dyes [6], pesticides [7]. Many treatment methods have been investigated for treating these contaminants such as precipitation using additive chemicals, adsorption using porous materials [3,8], bacterial activity process [5], membrane systems [9], oxidation process [4], and photocatalytic process using potential materials [7,10,11]. Among these, the photocatalytic process with wide band gap materials is considered a very interesting method for wastewater treatment because it can naturally occur under sunlight. Wide band gap materials such as TiO_2, CeO_2, Fe_3O_4, CdS, and ZnO have been investigated [12-15]. ZnO is one of the interesting photocatalytic materials for wastewater treatment due to its unique physicochemical, electrical, and optical properties [16]. It is a direct wide band gap semiconductor that has high carrier concentration and mobility, and it is suitability for nanostructure preparation [17-20]. The conventional band gap of ZnO is around 3.37 eV which can be excited by natural sunlight in the ultraviolet (UV) region for photocatalytic activation [16,21]. Brief description of the photocatalytic process, ZnO absorbs sunlight energy to generate electron-hole pairs. The pairs continuously diffuse to material surfaces and react with surrounding contaminants in wastewater for the photocatalytic treatment process. During the pair generation, the high carrier concentration and high mobility of ZnO can provide charge carrier diffusion and movement to the surfaces resulting in a high reaction rate for contaminant degradation [22]. Moreover, ZnO can be easier achieved in surface area by reducing particle size to nanostructures. The large surface area of the nanostructures can increase interfacial contact between the photocatalytic materials and

---

[*] Corresponding author: sutthipoj.s@gmail.com

surrounding contaminants. The improved high active surface area due to the increased interfacial contact can provide better treatment with high efficiency and short treatment time. However, the high purity of the ZnO crystal structure with low defects may not be suitable for photocatalytic application because carrier activity is not allowed due to the extreme crystal stability. On the other hand, lower stability may shorten the usability time under UV light excitation. Thus, ZnO with the appropriate balancing of pure and defect structures should be investigated.

In this research, clustered ZnO nanoparticles were synthesized using simple chemical precipitation. Zinc acetate dihydrate and ammonium bicarbonate were selected as low-cost starting materials. The synthesized ZnO was characterized using a variety of analytical techniques. Then, it was used as a photocatalytic material to treat wastewater carrying methyl orange or commercial glyphosate under ultraviolet (UV) activation. Finally, the photocatalytic performance was evaluated.

2. Experimental

2.1. Synthesis of clustered ZnO nanoparticles

Zinc acetate dihydrate ($Zn(CH_3COO)_2.2H_2O$) and ammonium bicarbonate (NH_4HCO_3) were used as starting materials. The starting materials were separately dissolved into distilled water under stirring at room temperature to form $Zn^{2+}$and OH^{-} aqueous solutions, respectively. The $Zn(CH_3COO)_2.2H_2O$ concentration was fixed at 0.4 M, and the NH_4HCO_3 concentration was varied (0.3, 0.4, and 0.5 M). After 1 h of stirring, the zinc acetate solution was heated at 70 °C for 15 min before the mixing process. Then, the ammonia solution was added drop by drop into the zinc acetate solution. The mixtures were continuously heated for 1 h under violent stirring. After cooling to room temperature, the obtained white product was collected and washed with distilled water several times. The product was then filtered through filter paper for 12 h, heated at 70 °C for 1 h, and ground. Finally, it was calcined at 550 °C for 1 h to obtain ZnO. The ZnO has grounded again before being kept in a brown bottle in the dark.

2.2. Characterization of ZnO

The synthesized ZnO was characterized using various analytical methods. Morphology was observed using scanning electron microscopy (SEM). The particle size distribution of the synthesized product was measured using a dynamic light scattering (DLS) technique by dispersing the synthesized ZnO into distilled water. The chemical composition was examined using wavelength dispersive spectroscopy (WDS). Chemical structures were examined using Fourier-transform infrared spectroscopy (FTIR). Molecular vibration was investigated using Raman spectroscopy. The crystal structure was characterized using X-ray diffraction (XRD). The optical band gap (E_g) was evaluated from transmittance which was measured using ultraviolet-visible (UV-Vis) spectroscopy.

2.3. Test of photocatalytic activity

The photocatalytic performance of the synthesized ZnO was evaluated from the degradation performance of representative wastewater carrying methyl orange or commercial glyphosate. The wastewater was prepared by dissolving methyl orange (1 mg) or commercial glyphosate (1 mL) into 100 mL distilled water, stirring for 30 min in the dark at room temperature. The photocatalytic test was performed by adding 0.1 g ZnO into the methyl orange solution or adding 0.2 g ZnO into the glyphosate solution. The ZnO was dispersed under sonication for 10 min in the dark. After the dispersion, the solutions were continuously kept in the dark for 30 min to maintain adsorption-desorption equilibrium. Then, the photocatalytic mechanism was activated under UV illumination (λ~365 nm, 1.6 mW/cm^2) for 150 min. Photocatalytic degradation was examined by measuring absorbances of the solutions after the UV illumination. Approximately 1.5 mL of the solutions were taken for absorbance measurement every 30 min. The photocatalytic performance was evaluated in terms of degradation efficiency and degradation rate constant using the pseudo-first-order kinetics.

3. Results and discussion

The morphology of the synthesized ZnO is shown in Fig. 1. Clustered ZnO nanoparticles are observed for all conditions and particle sizes likely increase as increasing $\mathrm{OH^-}$ concentration. The 0.3 M condition reveals that small nanoparticles accumulate to form smaller clusters, while 0.4 M and 0.5 M conditions show larger clusters. The results may occur due to the complete reaction because $\mathrm{Zn^{2+}}$ ions have higher concentration than $\mathrm{OH^-}$ ions in the case of 0.3 M condition. Thus, all $\mathrm{OH^-}$ ions are completely reacted with $\mathrm{Zn^{2+}}$ to form ZnO in a short duration according to Eq. (1)-(4) [23].

$$\mathrm{Zn(CH_3COO)_2 \cdot 2H_2O \rightarrow Zn^{2+} + 2CH_3COO^- + 2H_2O} \tag{1}$$

$$\mathrm{NH_4HCO_3 \rightarrow NH_4^+ + OH^- + CO_2} \tag{2}$$

$$\mathrm{Zn^{2+} + 2OH^- \rightarrow Zn(OH)_2} \tag{3}$$

$$\mathrm{Zn(OH)_2 \rightarrow ZnO + H_2O} \tag{4}$$

This effect leads to low accumulation on ZnO surfaces due to the low remaining $\mathrm{OH^-}$ ions. This effect can perform the small nanoparticle formation with small cluster accordingly [24]. On the other hand, remaining $\mathrm{OH^-}$ ions may react with the formed ZnO surfaces again in the case of high $\mathrm{OH^-}$ concentration causing accumulation to form large clusters can see in Fig. 1.

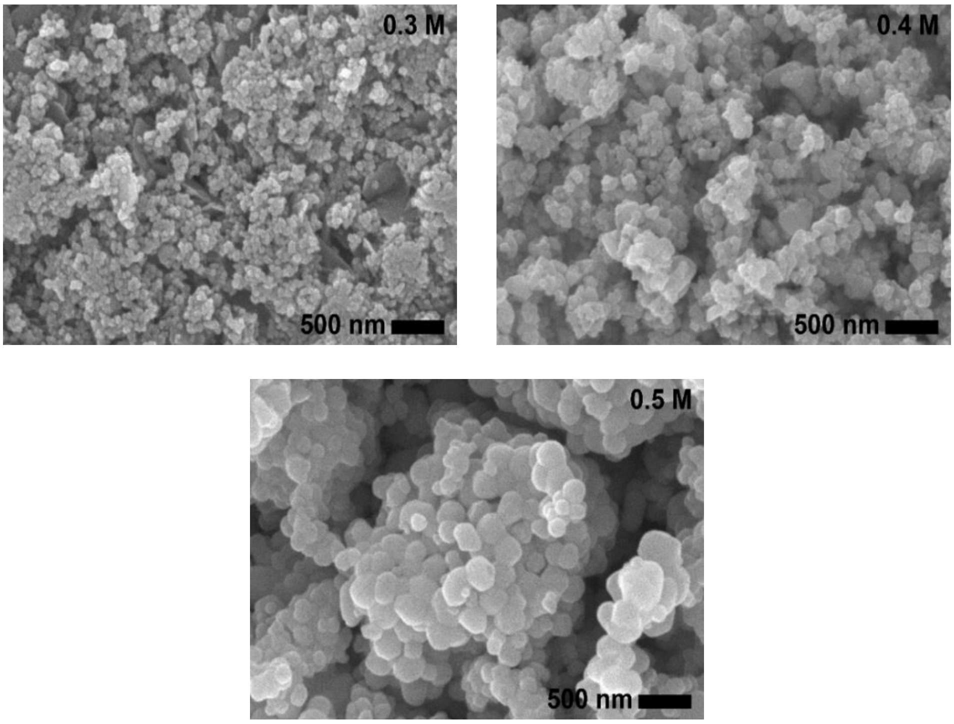

Fig. 1. Morphology of ZnO synthesized with different OH^- concentrations.

Dynamic light scattering (DLS) was performed to analyze particle sizes as shown in Fig. 2. It is found that all synthesized ZnO nanoparticles are composed of many sizes as can see in a wide range of the particle size distribution curve. The 0.3 M condition shows two dominant distribution peaks in ranges of around 0.4 – 10 nm and 100 – 1100 nm. The 0.4 M condition not only reveals distribution peaks as same as to the 0.3 M condition but also displays a peak around 1200 – 1600 nm. For the 0.5 M condition, only one range of particle size (110 – 1600 nm) is observed. It could interpret that small particle sizes can form for lower OH^- concentration (0.3 M and 0.4 M conditions). On the other hand, large particle sizes could be forming due to the remaining OH^- ions during the precipitation reaction. Therefore, it can conclude that small nanoparticles with small cluster can appropriately synthesis using a low OH^- concentration to avoid accumulation effect due to remaining OH^- ions.

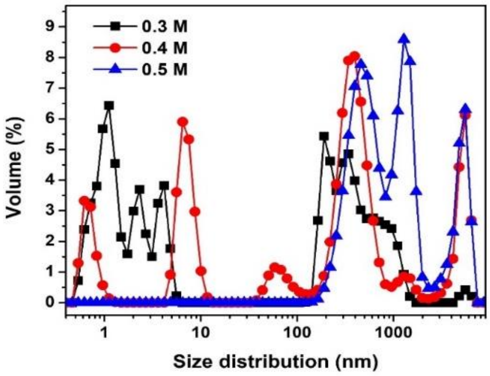

Fig. 2. Particle size distribution of ZnO synthesized with different OH^- concentrations.

Fig. 3 shows wavelength dispersive spectroscopy (WDS) of the clustered ZnO nanoparticles for chemical composition investigation. The Zn and O peaks are detected for all conditions indicating the fair ZnO purity [25]. Besides, the number of oxygens slightly increases in the correlation with the increasing OH^- concentration. This could have resulted from the rich OH^- ions implying defect formation.

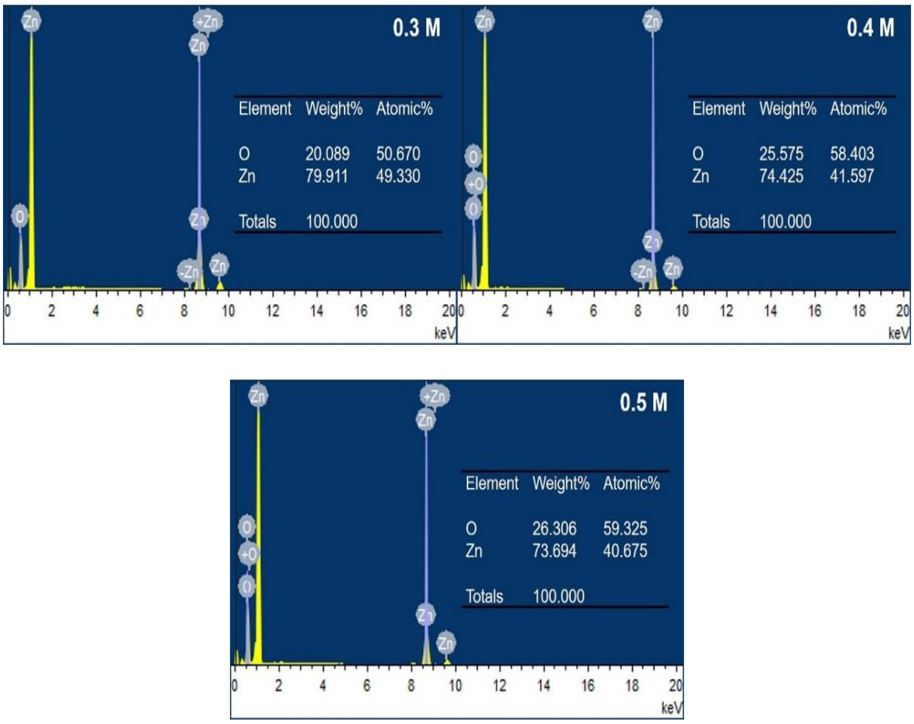

0.3 M

Element	Weight%	Atomic%
O	20.089	50.670
Zn	79.911	49.330
Totals	100.000	

0.4 M

Element	Weight%	Atomic%
O	25.575	58.403
Zn	74.425	41.597
Totals	100.000	

0.5 M

Element	Weight%	Atomic%
O	26.306	59.325
Zn	73.694	40.675
Totals	100.000	

Fig. 3. WDS of ZnO synthesized with different OH^- concentrations.

To investigate chemical structure of the clustered ZnO nanoparticles, FTIR measurement was performed as shown in Fig. 4. It is seen that the strong peak at wavenumber around 503-510 cm^{-1} is explored indicating Zn–O stretching vibration [26]. Due to the dominant single peak observation, it confirms the ZnO formation for all conditions. Note to the dominant peak, it slightly shifts to lower wavenumber for higher concentration conditions involving lower vibrational frequency between Zn and O. This behavior could be occurred due to richer oxygen sources. In addition, small peaks around 1559 cm^{-1} (C=O) and 3779 cm^{-1} (O–H) are appeared suggesting the chemical structure defects agree with the WDS result [27]. However, the very low peak intensity can be assumed to the extremely low defects for all condition.

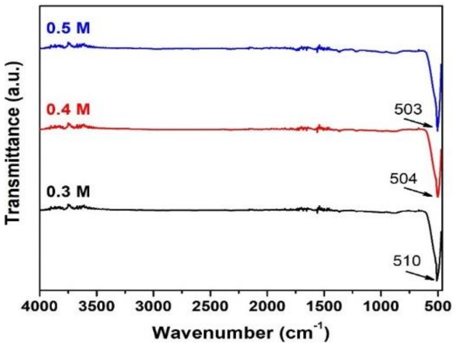

Fig. 4. FTIR spectra of clustered ZnO nanoparticles synthesized with different OH^{-} *concentrations.*

To investigate the defects which cannot be detected using WDS or FTIR, the molecular vibration of the clustered ZnO nanoparticles was examined using the Raman spectroscopy as shown in Fig. 5. The hexagonal wurtzite structure of ZnO is confirmed from three major vibration modes in the Raman spectrum located at 331 cm^{-1}, 382 cm^{-1}, and 437 cm^{-1}. The weak peak at 331 cm^{-1} and 382 cm^{-1} assigned to the multi-phonon vibration of E_2(high)-E_2(low) mode, and A_1(TO) mode, respectively. Note that, the weak peak of E_2(high)-E_2(low) mode indicates a low E_2(low) signaled to wurtzite ZnO which may be caused by the single crystal formation [28]. The strong peak at 437 cm^{-1} ascribed to the non-optical phonon E_2(high) mode which attributes the wurtzite structure of the clustered ZnO nanoparticles [29]. The observed peak located around 584 cm^{-1} was identified as the E_1(LO) mode. The peak shifts from the bulk structure formation (591 cm^{-1}) which refers to defects such as oxygen vacancy, zinc interstitials, or structural defects [30]. The defect ratio can be evaluated from the peak intensity at 584 cm^{-1} divided by the sum of peak intensity at 584 cm^{-1} and 437 cm^{-1} peaks ($I_{584}/(I_{584}+I_{437})$) [28]. It is found that the defect ratios are 0.167, 0.156, and 0.166 for the OH^{-} concentration of 0.3 M, 0.4 M, and 0.5 M, respectively, which are not many differences.

The crystal structure is considered from the XRD measurement as shown in Fig. 6. Diffraction peaks at crystal plans of (100), (002), (101), (102), (110), (103), (200), (112) and (201) are explored at diffraction angle 2θ around 31.78°, 34.44°, 36.28°, 47.58°, 56.64°, 62.92°, 66.44°, 68.00° and 69.02°, respectively. These peaks correspond to the hexagonal wurtzite structure (JCPDS card no. 36-1451) [31]. To evaluate crystal size (D) and dislocation density (δ), the three major plans of (100), (002) and (101) were calculated using the Eq. (5)-(6), respectively [7,27,32].

$$\mathrm{D} = \frac{\mathrm{k}\lambda}{\beta\cos\theta} \tag{5}$$

$$\delta = \frac{1}{\mathrm{D}^2} \tag{6}$$

k is the constant of XRD measurement system (0.89), λ is the wavelength of X-ray source (1.5406 Å), β is full-width at the half-maximum (FWHM) intensity, and θ is the diffraction angle.

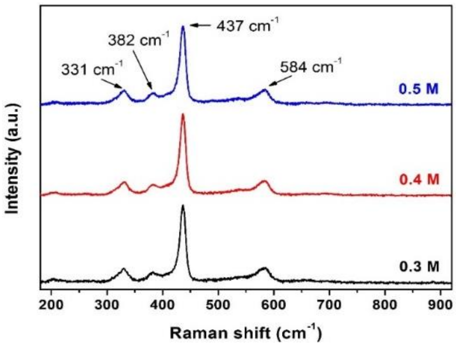

Fig. 5. Raman shift of ZnO synthesized with different OH^- concentrations.

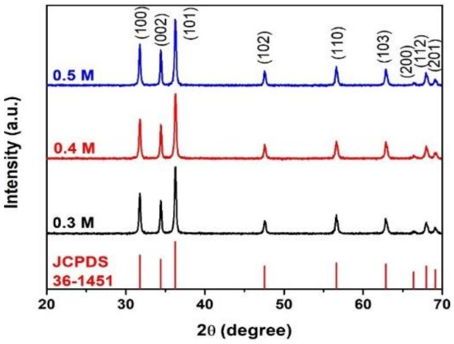

Fig. 6. XRD patterns of ZnO synthesized with different OH^- concentrations.

It is found that the average crystal size slightly increases as increasing $\mathrm{OH^-}$ concentration as listed in Table 1, suggesting the nanocrystal formation for all conditions. The dislocation density is decreased which agrees to the large crystal size and better crystallization. For crystal analysis, lattice constants ‘a’ and ‘c’ were calculated using Eq. (7)-(8) from the plans of (100) and (002), respectively. Interplanar-spacing (d_{hkl}) was calculated using Eq. (7)-(9) [7,27,32,33].

$$\mathrm{a} = \frac{\lambda}{\sqrt{3}\sin\theta} \tag{7}$$

$$\mathrm{c} = \frac{\lambda}{\sin\theta} \tag{8}$$

$$2\mathrm{d_{hkl}}\sin\theta = \mathrm{n}\lambda \tag{9}$$

h,k,l are miller indices, and n is 1 for the first-order diffraction. From the calculation in Table 1, it is found that there are very few different values of lattice constants for all conditions. Likewise, interplanar-spacing also shows similar values. These values are close to the standard JCPDS values (a = 3.250 Å, c = 5.207 Å, d_{100} = 2.814 Å, d_{101} = 2.603 Å) implying high crystallinity of clustered ZnO nanoparticles with very low crystal defects such as oxygen vacancy. In addition to growth direction analysis, the texture coefficient (T_c) of plans (100) and (002) was calculated according to Eq. (10) [7,27].

$$T_{c(hkl)} = \frac{\frac{I_{(hkl)}}{I_{0(hkl)}}}{\frac{1}{N}\sum\frac{I_{(hkl)}}{I_{0(hkl)}}} \tag{10}$$

$I_{0(hkl)}$ is the standard intensity of the preferred orientation plane from JCPDS, and N is the number of considered plans. It is found that the 0.3 M condition shows little different values between $T_{c(100)}$ and $T_{c(002)}$. This result refers that growth rates in a-axis and c-axis are symmetry, indicating spherical growth. For other conditions, $T_{c(002)}$ exhibits larger than $T_{c(100)}$ indicating c-axis direction growth of rod-like structure. However, the synthesizing process of precipitation reaction without direction control could not appropriate for complete rod growth. So, accumulation has appeared in this case.

Table 1. Crystal characteristics of clustered ZnO nanoparticles.

OH^- concentration	D (nm)	δ (nm^{-2})	a (Å)	c (Å)	d_{100}	d_{002}	$T_{c(100)}$	$T_{c(002)}$
0.3 M	45.254	5.04×10^{-4}	3.247	5.206	2.812	2.603	1.230	1.280
0.4 M	46.793	4.68×10^{-4}	3.250	5.204	2.814	2.602	1.150	1.364
0.5 M	55.694	4.30×10^{-4}	3.248	5.210	2.813	2.605	1.215	1.367

Optical band gap (E_g) was estimated from optical transmittance using the Tauc's plot according to the relation [6,34,35].

$$\alpha h\nu = A\left(h\nu - E_g\right)^n \tag{11}$$

α and A are constants, h is the Plank's constant, ν is frequency, and n is ½ for direct band gap semiconductors as for the case of ZnO. The $(\alpha h\nu)^2$ versus hν graph is plotted as shown in Fig. 7. The graph was analyzed by linear fitting and E_g was estimated from the interception point on the hν-axis as shown in Table 2. The lowest E_g is presented for the 0.3 M condition, and E_g is obtained in a very small range (3.06 – 3.16 eV) similar with elsewhere reports [6,36,37]. The different E_g values may have been due to diverse factors such as carrier concentration, particle size, and defects [14]. It is found that the calculated E_g values show a red shift in comparison to common ZnO (3.37 eV) [38,39], correlating to the defect ratios from the Raman results. The red shift effect could be considered as a better characteristic for extending absorption wavelength covering both the UV and visible light regions [38].

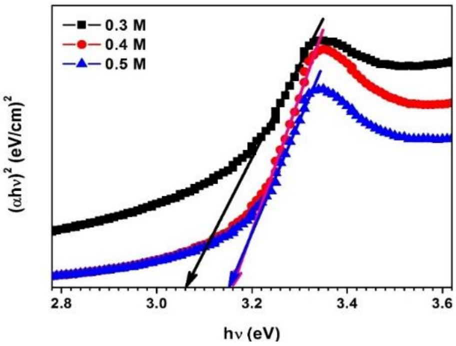

Fig. 7. The $(\alpha h\nu)^2$ versus $h\nu$ graph of clustered ZnO nanoparticles synthesized with different OH^- concentrations.

Table 2. Optical band gap of clustered ZnO nanoparticles.

OH^- concentration	E_g (eV)	R^2
0.3 M	3.06	0.9892
0.4 M	3.16	0.9893
0.5 M	3.15	0.9895

To investigate photocatalytic degradation, clustered ZnO nanoparticles were dispersed into methyl orange or glyphosate solutions. The photocatalytic mechanism was then activated under UV illumination. For irradiation interval time, solutions were tracked out for absorbance measurement as shown in Fig. 8 and Fig. 9. It is found that absorbance spectra decrease as increasing irradiation time for all conditions referring to the degradation of contaminant molecules (methyl orange or glyphosate). This phenomenon occurs because contaminant molecules had degraded during the photocatalytic process according to the relation [10,11,37,40].

$$\mathrm{ZnO} + \mathrm{h\upsilon} \rightarrow \mathrm{ZnO} + \mathrm{e}^{-(\mathrm{CB})} + \mathrm{h}^{+(\mathrm{VB})} \tag{12}$$

$$\mathrm{H_2O} \rightarrow \mathrm{OH}^- + \mathrm{H}^+ \tag{13}$$

$$\mathrm{OH}^- + \mathrm{h}^{+(\mathrm{VB})} \rightarrow \mathrm{OH}^{\cdot} \tag{14}$$

$$\mathrm{O_2} + \mathrm{e}^{-(\mathrm{CB})} \rightarrow \mathrm{O}_2^{\cdot -} \tag{15}$$

$$\text{Contaminants} + \mathrm{OH}^{\cdot} \rightarrow \text{other products} \tag{16}$$

$$\text{Contaminants} + \mathrm{O}_2^{\cdot -} \rightarrow \text{other products} \tag{17}$$

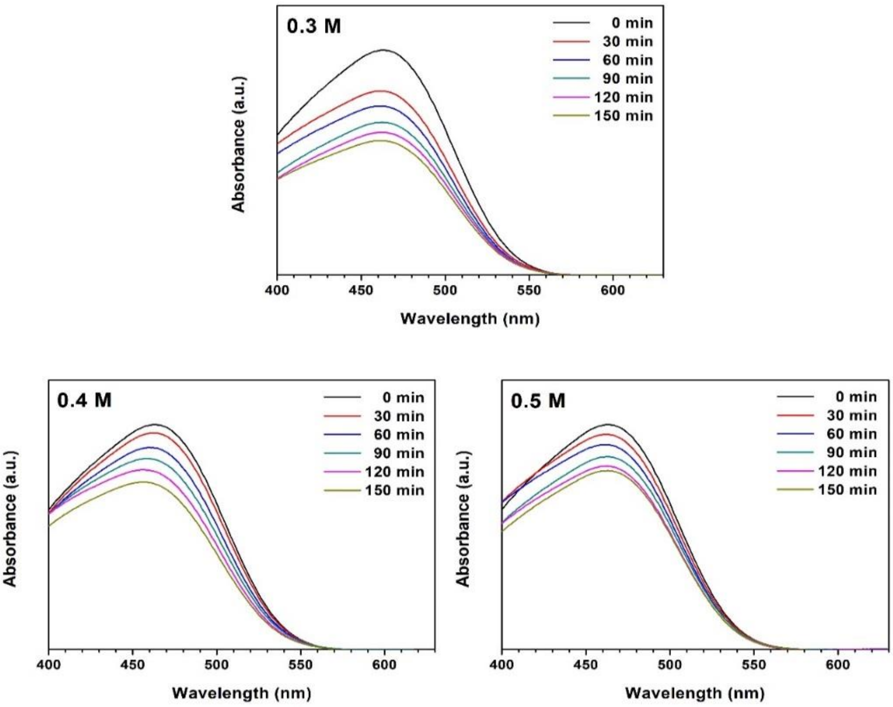

Fig. 8. Absorbance of methyl orange solution after photocatalytic degradation for interval time with clustered ZnO nanoparticles synthesized at different OH^- concentrations.

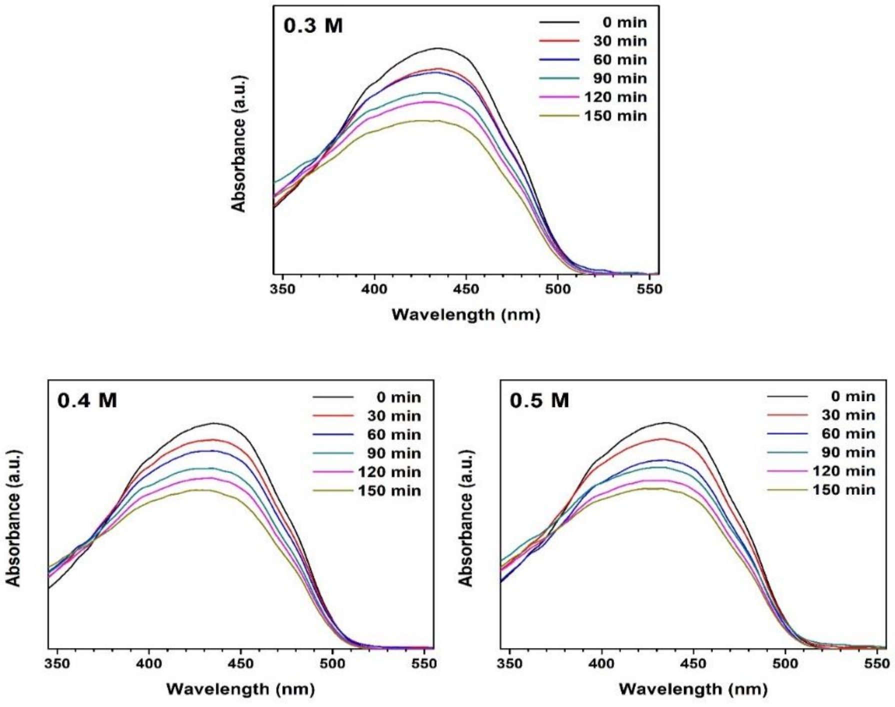

Fig. 9. Absorbance of glyphosate solution after photocatalytic degradation for interval time with clustered ZnO nanoparticles synthesized at different OH^- *concentrations.*

The mechanism of photocatalytic degradation can accordingly describe. After electron-hole pair generation, the reaction between the pairs and surrounding intermediates causes $\mathrm{OH}^{\cdot}$ and $\mathrm{O}_2^{\cdot-}$ radicals. Then, the radicals continuously react with contaminant molecules for the degradation process. The contaminant molecules are decomposed and transformed into other products such as water, minerals, and carbon dioxide [23,24,41]. To evaluate degradation performance, the degradation efficiency (DE) of methyl orange and glyphosate was calculated using the relation [7,23].

$$\mathrm{DE}(\%) = \left(\frac{\mathrm{C_0 - C}}{\mathrm{C_0}}\right) \times 100\% = \left(\frac{\mathrm{A_0 - A}}{\mathrm{A_0}}\right) \times 100\% \tag{18}$$

C_0 and C are concentrations at the initial time (t = 0 min) and interval irradiation time, respectively. Likewise, A_0 and A are absorbances at the initial time, and interval irradiation time, respectively. In this case, degradation efficiency was evaluated from the absorbance peak because it is well-known that concentration and absorbance are in the directing correlation. The absorbance values were tracked from the maximum absorbance peak at the wavelength of 465 nm and 435 nm for methyl orange and glyphosate, respectively [7,42]. The degradation efficiency shows different values for each clustered ZnO nanoparticle samples (Fig. 10). The dominant degradation efficiency of methyl orange is found for the 0.3 M condition and this had higher performance than other conditions. For glyphosate, it is difficult to determine the best degradation efficiency because degradation efficiency graphs are not significant differences. Thus, the graph of ln (A/A_0) versus irradiation time was plotted (Fig. 11) for quantitative analysis in terms of kinetic parameters. The kinetic parameters of photocatalytic degradation were evaluated using pseudo-first-order kinetics in Eq. (19) and listed in Table 3.

$$\ln\left(\frac{\mathrm{A}}{\mathrm{A_0}}\right) = -\mathrm{k_r t} \tag{19}$$

k_r and t are the degradation rate constant and irradiation time, respectively. The k_r can be estimated from the slope of the graph. The half-life value (τ) was also estimated in correspondence to the decomposition of contaminant concentration to one-half of the initial concentration. Generally, high k_r and low τ are expected for fast degradation and short irradiation time, respectively. It is found that the 0.3 M condition presents the maximum k_r for both methyl orange and glyphosate indicating the highest photocatalytic activity to decompose contaminant molecules from the wastewater. Furthermore, the minimum τ suggests a shorter irradiation time to 50% decomposition of the dissolved contaminant molecules. Thus, the best photocatalytic performance of methyl orange or glyphosate is concluded for the clustered ZnO nanoparticles synthesized with low OH^- concentration. This behavior may cause by the high active surface area due to small particle size formation [23,43]. According to the size distribution, the 0.3 M condition shows higher particle size distribution in the range of 0.4 – 10 nm compared with 0.4 M and 0.5 M conditions. Moreover, high dislocation density due to low crystal size could act as interaction centers for accelerating photocatalytic activity at the same time. Note to the red shift in optical band gap, it might reduce the required exciting energy for electron-hole pair generation which also easily activates photocatalytic activity. Therefore, it is believed that the best photocatalytic performance is caused by the synergy of small particle sizes, small crystal sizes, high dislocation density, and low optical band gap.

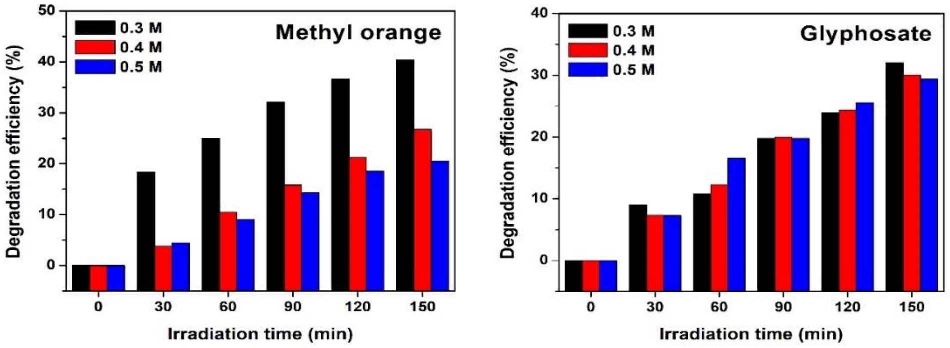

Fig. 10. Degradation efficiency of methyl orange and glyphosate.

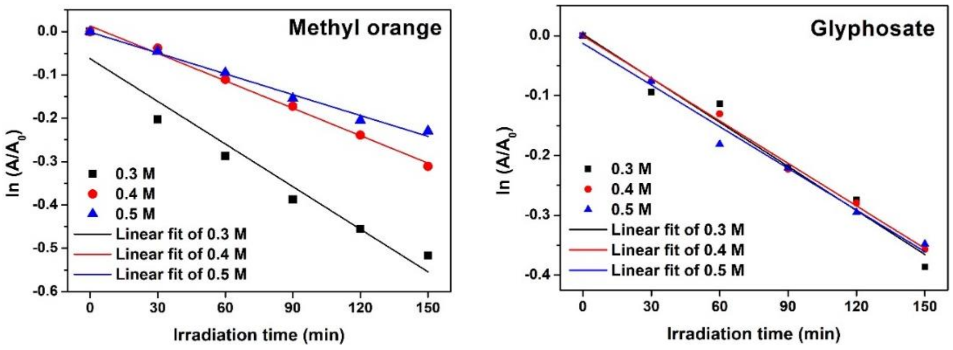

Fig. 11. Plots of ln(A/A_0) versus irradiation time of methyl orange and glyphosate.

Table 3. Kinetic parameters of photocatalytic degradation.

OH^- concentration	Methyl orange			Glyphosate		
	k_r (min^{-1})	τ (min)	R^2	k_r (min^{-1})	τ (min)	R^2
0.3 M	3.28×10^{-3}	211	0.9387	2.45×10^{-3}	283	0.9708
0.4 M	2.11×10^{-3}	329	0.9929	2.37×10^{-3}	292	0.9960
0.5 M	1.60×10^{-3}	433	0.9888	2.32×10^{-3}	299	0.9818

4. Conclusions

Synthesis of clustered ZnO nanoparticles was performed using simple chemical precipitation with low-cost starting materials (zinc acetate dihydrate and ammonium bicarbonate). The morphological and particle size analyses show the cluster formation of nanoparticles. Small particles are observed at the low $\mathrm{OH^-}$ concentration due to very little remaining $\mathrm{OH^-}$ ions during precipitation reaction. The ZnO formation is detected according to the Zn and O peaks. The hexagonal wurtzite structure is confirmed by Raman shift, FTIR, and XRD diffraction. High crystallinity of hexagonal wurtzite structure is observed according to the similar crystal characteristics including lattice constants and interplanar-spacing. Moreover, these crystal parameters are close to the standard JCPDS. However, the clustered ZnO nanoparticles synthesized from low $\mathrm{OH^-}$ concentration exhibits the lowest crystal size and highest dislocation density. Moreover, the crystal growth direction is preferred to (100) and (002) plans indicating the spherical growth. Optical band gap is in a small range with red shift in comparison with common ZnO.

For photocatalytic degradation of methyl orange or commercial glyphosate, the best photocatalytic performance is found with the maximum degradation rate constant of 3.28×10^{-3} min^{-1} and 2.45×10^{-3} min^{-1} for methyl orange and glyphosate, respectively. The best photocatalytic performance is caused by synergy of small particle sizes, small crystal sizes, high dislocation density, and low optical band gap. Therefore, clustered ZnO nanoparticles synthesized by precipitation with low-cost starting materials demonstrate a potential photocatalytic material to decompose methyl orange and glyphosate. Furthermore, it might be also considered for agricultural area application.

Acknowledgments

This work was supported by the Kasetsart University Research and Development Institute (KURDI), Kasetsart University, Bangkok, Thailand. Authors would like to kindly acknowledge the Department of Physics, Faculty of Liberal Arts and Science, Kasetsart University Kamphaeng Saen Campus, Nakhon Pathom, Thailand for facilities.

References

[1] A. Ramirez, S. Giraldo, J. García-Nunez, E. Flórez, N. Acelas, Journal of Water Process Engineering **26**, 131 (2018).

[2] Q. Xi, G. Gao, M. Jin, Y. Zhang, H. Zhou, C. Wu, Y. Zhao, L. Wang, P. Guo, J. Xu, Applied Surface Science **471**, 714 (2019).

[3] M. S. Tizo, L. A. V. Blanco, A. C. Q. Cagas, B. R. B. Dela Cruz, J. C. Encoy, J. V. Gunting,

R. O. Arazo, V. I. F Mabayo, Sustainable Environment Research **28**, 326 (2018).

[4] F. C. Moreira, R. A. R. Boaventura, E. Brillas, V. J. P. Vilar, Applied Catalysis B: Environmental **202**, 217 (2017).

[5] M. Lindroos, D. Hörnström, G. Larsson, M. Gustavsson, A. J. A. van Maris, Journal of Hazardous Materials **365**, 74 (2019).

[6] M. Zarrabi, M. Haghighi, R. Alizadeh, Ultrasonics Sonochemistry **48**, 370 (2018).

[7] S. Phophayu, P. Pimpang, S. Wongrerkdee, S. Sujinnapram, S. Wongrerkdee, Journal of Reinforced Plastics and Composites **39**, 81 (2020).

[8] Y. D. Liang, Y. J. He, T. T. Wang, L. H. Lei, Journal of Water Process Engineering **27**, 77 (2019).

[9] M. Aslam, A. Charfi, G. Lesage, M. Heran, J. Kim, Chemical Engineering Journal **307**, 897 (2017).

[10] X. Li, C. Wang, N. Xia, M. Jiang, R. Liu, J. Huang, Q. Li, Z. Luo, L. Liu, W. Xu, D. Fang, Journal of Molecular Structure **1148**, 347 (2017).

[11] A. H. Mamaghani, F. Haghighat, C. S. Lee, Applied Catalysis B: Environmental **203**, 247 (2017).

[12] C. Santhosh, V. Velmurugan, G. Jacob, S.K. Jeong, A.N. Grace, A. Bhatnagar, Chemical Engineering Journal **306**, 1116 (2016).

[13] P. Zhang, X. Li, X. Wu, T. Zhao, L. Wen, Journal of Alloys and Compounds **673**, 405 (2016).

[14] S. Bhatia, N. Verma, Materials Research Bulletin **95**, 468 (2017).

[15] S. Tambat, S. Umale, S. Sontakke, Integrated Ferroelectrics **186**, 54 (2018).

[16] C. Yao, J. Zhu, H. Li, B. Zheng, Y. Wei, Russian Journal of Physical Chemistry A **91**, 2680 (2017).

[17] P. Pimpang, A. S. Zoolfakar, R. A. Rani, R. A. Kadir, D. Wongratanaphisan, A. Gardchareon, K. Kalantar-zadeh, S. Choopun, Ceramics International **43**, S511 (2017).

[18] P. Ruankham, D. Wongratanaphisan, A. Gardchareon, S. Phadungdhitidhada, S. Choopun, T. Sagawa, Applied Surface Science **410**, 393 (2017).

[19] E. Wongrat, W. Ponhan, S. Choopun, Ceramics International **43**, S520 (2017).

[20] B. K. Singh, S. Tripathi, Journal of Luminescence **198**, 427 (2018).

[21] T. Shibata, K. Yamamoto, J. Sasano, M. Nagai, AIP Advances **7**, 095012 (2017).

[22] H. Makino, H. Shimizu, Applied Surface Science **439**, 839 (2018).

[23] S. Moungsrijun, S. Sujinnapram, S. Sutthana, Monatshefte fur Chemie **148**, 1177 (2017).

[24] N. Tripathy, R. Ahmad, H. Kuk, D. H. Lee, Y. B. Hahn, G. Khang, Journal of Photochemistry and Photobiology B: Biology **161**, 312 (2016).

[25] M. F. Ehsan, S. Bashir, S. Hamid, A. Zia, Y. Abbas, K. Umbreen, M. N. Ashiq, A. Shah, Applied Surface Science **459**, 194 (2018).

[26] M. M. Ba-Abbad, A. A. H. Kadhum, A. B. Mohamad, M. S. Takriff, K. Sopian, Journal of Alloys and Compounds **550**, 63 (2013).

[27] S. Krobthong, S. Wongrerkdee, Journal of Metals, Materials and Minerals **30**, 38 (2020).

[28] Z. Yu, H. Moussa, Y. Ma, M. Liu, B. Chouchene, R. Schneider, M. Moliere, H. Liao, Journal of Colloid and Interface Science **534**, 637 (2019).

[29] R.S. Ganesh, G. K. Mani, R. Elayaraja, E. Durgadevi, M. Navaneethan, S. Ponnusamy, K. Tsuchiya, C. Muthamizhchelvan, Y. Hayakawa, Applied Surface Science **449**, 838 (2018).

[30] N. A. Hammed, A. A. Aziz, A. I. Usman, M. A. Qaeed, Ultrasonics Sonochemistry **50**,

172 (2019).

[31] S. Wongrerkdee, S. Moungsrijun, S. Sujinnapram, S. Krobthong, S. Choopun, Bulletin of Materials Science **42**, 91 (2019).

[32] S. Krobthong, S. Nilphai, S. Choopun, S. Wongrerkdee, Digest Journal of Nanomaterials and Biostructures **15**, 885 (2020).

[33] P. Suttiyarak, S. Buathet, A. Tubtimtae, Optik **212**, 164662 (2020)

[34] T. Chankhanittha, S. Nanan, Materials Letters **226**, 79 (2018).

[35] A. Kumar, S. Billa, S. Chaudhary, A. B. V. K. Kiran Kumar, C. V. V. Ramana, D. Kim, Inorganic Chemistry Communications **97**, 191 (2018).

[36] M. A. Ciciliati, M. F. Silva, D. M. Fernandes, M. A. C. de Melo, A. A. W. Hechenleitner, E. A. G. Pineda, Materials Letters **159**, 84 (2015).

[37] A. Kaur, G. Gupta, A. O. Ibhadon, D. B. Salunke, A. S. K. Sinha, S. K. Kansal, Journal of Environmental Chemical Engineering **6**, 3621 (2018).

[38] A. Hosseini, H. Faghihian, A. M. Sanati, Materials Science in Semiconductor Processing **87**, 110 (2018).

[39] W. L. Liu, Y. F. Zhang, Integrated Ferroelectrics **188**, 112 (2018).

[40] B. Dindar, A. C. Güler, Environmental Nanotechnology, Monitoring and Management **10**, 457 (2018).

[41] M. Zangiabadi, T. Shamspur, A. Saljooqi, A. Mostafavi, Applied Organometallic Chemistry **33**, e4813 (2019).

[42] X. Liu, H. Cheng, F. Fu, W. Huang, H. Zuo, L. Yan, L. Li, Materials Letters **179**, 134 (2016).

[43] M. Pirhashemi, A. Habibi-Yangjeh, Journal of Materials Science and Technology **34**, 1891 (2018).